Research Article

Ahmed M. Galal, Rania Saadeh, Adebowale Martins Obalalu, Umair Khan*, and Samia Elattar

Dissipative disorder optimization in the radiative thin film flow of partially ionized non-Newtonian hybrid nanofluid with second-order slip condition

https://doi.org/10.1515/phys-2025-0149
received January 19, 2025; accepted March 06, 2025

Abstract: The optimization of dissipative disorder in fluid dynamics is a critical aspect of enhancing heat and mass transport efficiency in advanced thermal applications. In this study, we investigate the radiative thin film flow of a partially ionized non-Newtonian hybrid nanofluid (HNF) under the influence of a second-order slip condition. The HNF comprises magnesium oxide (MgO) and zinc oxide (ZnO) nanoparticles (NPs) suspended in water, which enhances its thermophysical properties, including thermal conductivity and heat absorption capacity. HNFs exhibit superior thermal transport capabilities compared to conventional fluids; however, their flow behavior is highly complex, especially in the presence of ionization effects, radiative heat transfer, and interfacial slip dynamics. The second-order slip condition accounts for microscale effects, which are crucial for accurately modeling thin film flows in high-performance cooling and coating applications. The governing equations, incorporating the effects of viscoelasticity, solar radiation, Brownian motion, slip, unsteadiness, and magnetic field interactions, are formulated and solved using collocation weighted residual. The results indicate that incorporating MgO and ZnO NPs into the water base fluid enhances thermal conductivity, leading to improved heat transfer efficiency. The solar radiation parameter significantly increases the fluid temperature, leading to a stronger thermal boundary layer. The findings provide insight into minimizing dissipative losses while enhancing energy transport in industrial and aerospace systems. This study contributes to the advancement of HNF-based technologies by optimizing flow and heat transfer characteristics under complex physical conditions.

Keywords: Powell-Eyring fluid, liquid thin film flow, partially ionized, magnesium and zinc oxide

*** Corresponding author: Umair Khan**, Department of Mathematics, Saveetha School of Engineering, Saveetha Institute of Medical and Technical Sciences, Saveetha University, Chennai, 602105, Tamil Nadu, India; Department of Mathematics, Faculty of Science, Sakarya University, Serdivan/Sakarya, 54050, Turkey, e-mail: umairkhan@sakarya.edu.tr
Ahmed M. Galal: Department of Mechanical Engineering, College of Engineering in Wadi Alddawasir, Prince Sattam bin Abdulaziz University, Wadi Alddawasir, Saudi Arabia; Production Engineering and Mechanical Design Department, Faculty of Engineering, Mansoura University, P.O 35516, Mansoura, Egypt, e-mail: ahm.mohamed@psau.edu.sa
Rania Saadeh: Department of Mathematics, Faculty of Science, Zarqa University, Zarqa, 13110, Jordan, e-mail: rsaadeh@zu.edu.jo
Adebowale Martins Obalalu: Department of Mathematics and Statistics, Kwara State University, Malete, Nigeria, e-mail: adebowale.obalalu17@gmail.com
Samia Elattar: Department of Industrial and Systems Engineering, College of Engineering, Princess Nourah bint Abdulrahman University, P.O. Box 84428, Riyadh, 11671, Saudi Arabia, e-mail: SAElattar@pnu.edu.sa

Nomenclature

$\widetilde{T}$	temperature of the HNF
$\widetilde{C}$	concentration of nanoparticles
$\widetilde{C}_{\mathrm{s}}$	wall concentration
q_{r}	radiative heat flux
k^*	Rosseland mean absorption coefficient
σ^*	Stefan-Boltzmann constant
Q^*	non-uniform energy source
A, B	heat source and heat sink parameters
x, y	Cartesian coordinates
μ_{unf}	dynamic viscosity of the HNF
ρ_{unf}	density of the HNF
k_{unf}	thermal conductivity of the HNF
σ_{unf}	electrical conductivity of the HNF
$(\rho C_{\mathrm{p}})_{\mathrm{unf}}$	heat capacity of the HNF
$\xi_{\mathrm{H}}, \xi_{\mathrm{i}}$	hall and ion slip parameters
B_0	magnetic field strength
δ	material parameter
ϱ	second material parameter
d, a	arbitrary constants
u_w	wall velocity
u_{slip}	velocity slip
D_{T}	thermophoretic diffusion coefficient

Open Access. © 2025 the author(s), published by De Gruyter. This work is licensed under the Creative Commons Attribution 4.0 International License.

ν_f	kinematic viscosity of the base fluid
k_f	thermal conductivity of the base fluid
$\forall$	slip coefficient
h	height of the domain
$\frac{dh}{dt}$	rate of change of height

1 Introduction

Liquid thin film flow (LTFF) is a key concept in fluid dynamics, describing the movement of a thin liquid layer over a solid or fluid surface. This flow is governed by a balance of forces, including surface tension, viscous forces, gravity, and external influences such as thermal or electromagnetic fields [1–3]. The significance of LTFF lies in its widespread industrial and technological applications. One of the primary applications is in the coating and printing industry, where the uniform deposition of liquid films ensures the quality and performance of products such as paints, adhesives, and electronic displays. Thin film coatings are essential in microelectronics, photovoltaic cells, and biomedical implants, requiring precise control over film thickness and stability [4–6]. In thermal and energy systems, LTFF plays a crucial role in heat exchangers, cooling mechanisms, and evaporation-based technologies. The efficient heat transfer in thin liquid films is pivotal in enhancing the performance of condensers, refrigeration units, and solar thermal collectors. The study of thermophoretic particle deposition in thin films has also gained attention in optimizing energy conversion and environmental applications. Biomedical and microfluidic applications further underscore the importance of LTFF. In lab-on-chip devices, controlled thin film flows facilitate drug delivery, chemical reactions, and diagnostics. Biological thin films, such as tear films in ophthalmology, exhibit complex rheological properties that require advanced modeling techniques for medical advancements. Zhang *et al.* [7] explore the thermal and dynamic performance of a squeeze-film flow between two rotating disks. The analysis combines numerical simulation and experimental validation to understand how thermal transport influences the fluid system. They employ the finite-volume technique to solve the governing equations and confirm accuracy *via* testing for grid convergence and verifying energy conservation. The results provide insights into how thermal impact and surface geometry influence the performance and dynamics of lubrication systems in rotating machinery. This recent work of Zheng *et al.* [8] introduces a laminar two-dimensional (2D) model for LTFF, validated through experiment outcomes. It incorporates aluminum oxide nanoparticles (NPs) into water, ethylene glycol, and lithium bromide-water solution to increase thermophysical properties. Jiang *et al.* [9] investigate the thermal distribution, entropy generation, and performance of unsteady LTFF magnetohydrodynamic (MHD) nanofluid flow containing alumina and water over an inclined surface.

Partially ionized fluids (PIFs) are a class of fluids that contain both neutral and charged particles, typically composed of ions, electrons, and neutral atoms or molecules [10]. Unlike fully ionized plasmas, where all atoms are stripped of their electrons, PIFs exhibit a balance between neutral and charged species, leading to complex interactions influenced by electromagnetic forces, collisions, and thermal effects. These fluids are commonly found in astrophysical, industrial, and engineering applications, including fusion reactors, atmospheric phenomena, and space propulsion systems [11]. PIFs have critical applications in various scientific and engineering fields. In aerospace engineering, they play a vital role in ion thrusters and plasma propulsion systems, where controlled ionization enhances thrust efficiency. In astrophysics, they are essential in understanding stellar atmospheres, planetary ionospheres, and interstellar medium dynamics [12,13]. In nuclear fusion technology, partially ionized plasmas are significant in magnetically confined fusion devices (such as tokamaks and stellarators), where neutral particle interactions influence plasma stability and energy confinement [14]. Similarly, in industrial applications, PIFs are used in plasma-assisted manufacturing, semiconductor processing, and advanced material coatings [15]. The concept of PIFs in fluid dynamics is important since it fills a gap between fluid mechanics and plasma physics. They supply conceptual information needed on how electromagnetic forces influence fluids and their effectiveness in creating high technologies and estimating in nature. In addition, the investigation of the PIFs contributes toward the construction of new computational approaches and experimental procedures, which in turn provide more realistic forecasts of system behavior [16–18]. Iqbal *et al.* [19] used the homotopy analysis method to computationally investigate the Cattaneo–Christov heat flux and the behavior of gyrotactic microorganisms in the flow of a partially ionized hybrid nanofluid (HNF). Their result shows that radial velocity is reduced with increasing values of the magnetic field, Hall effect, ion slip, and material parameters. Also, the transverse velocity is enhanced with increasing values of magnetic field, Hall effect, ion slip, and material parameters. Jazaa *et al.* [20] presented a non-Newtonian Powell–Eyring fluids model that revealed the influence of PIF, slip, magnetic, and unsteadiness on the enhancement of thermal transport. The entropy-optimized performance of flow and thermal transport of a partially ionized, magnetically influenced Prandtl fluid enriched with three kinds of nanomaterials drifting across a convectively heated cylinder

were studied by Wang *et al.* [21]. They observed that the Hall and ion slip effects reduce entropy formation.

The investigation of HNFs is therefore an enhanced class of nanofluids, which comprise two or even more peculiar NPs dispersed in the base fluid for improving heat and fluid characteristics [22–24]. These nanofluids, augmented by mixing numerous kinds of NPs including metallic (gold, silver, iron, zinc oxide [ZnO]), non-metallic (graphene, CNTs), and ceramic (titanium dioxide, graphene oxide), possess advanced thermal conductivity, thermal transport efficiency, and stability than the regular nanofluids. HNFs offer numerous benefits over single-particle nanofluids, including low thermal performance enhancement, instability, and agglomeration [25]. On the one hand, the benefits expected from HNFs are countless. First, it can increase the thermal conductivity and the heat exchanging capability. Second, the HNFs have improved rheological features involving viscosity regulation of a flow. The HNFs are employed in numerous areas due to the fact that they are involved in controlling fluid dynamics and thermal transport [26]. They have been employed in car manufacturing, electronics, aerospace, and energy application sectors. For example, they are used in automobile cooling systems to raise the efficiency of engines, in electronics cooling systems to increase the dissipation of heat from high-density devices and in solar thermal systems to increase the efficiency of energy harvest and storage [27–29]. They are also employed in nuclear reactors, heating, ventilation, and air conditioning systems, and systems salient to biomedical uses like drug delivery and hyperthermia. Furthermore, they play an important function in the designation of energy savings and the optimization of the sustainability of industry processes. The combination of using carbon nanotubes and metal oxide NPs makes HNFs ideal for high-performance cooling and heating fluids for industries, which in future will determine the future of fluid dynamics and thermal engineering [30–32]. The work of Mishra and Pathak [31] inspects the hydro-thermal performance of molybdenum disulfide–silicon dioxide/water HNF and molybdenum disulfide–silicon dioxide–graphene oxide/water ternary HNF flowing over an inclined cylinder, considering heat generation/absorption effects. The outcomes describe that the thermal profiles are higher for the ternary HNF than HNF for increasing values of thermal radiation parameter and Eckert number. Also, the velocity profiles of both HNFs experience a reduction when higher values of suction/injection parameters are applied. The natural convection thermal transport of alumina–multiwalled carbon nanotube (Al_2O_3–MWCNT)/water HNF prepared *via* a two-step method at varying volume concentrations (0.00–0.20%) was studied by Scott *et al.* [32]. The numerical investigation of the flow and thermal performance of MgO–Al_2O_3/water HNF within a Darcy–Forchheimer–Brinkman framework under the influence of a horizontal magnetic field was conducted by Mebarek-Oudina *et al.* [33]. The outcomes show the increased pattern of the thermal and dynamical behavior of the HNF when augmenting the concentration, shape factor, porosity, and Darcy number; however, it also engenders increased formations of irreversibilities in the system that were revealed to enhance with the permeability and the great properties of the nanofluid. Nevertheless, this thermally enhanced pattern is shown to degrade with strong Hartmann values, which also reduced both thermal and viscous entropies.

The non-Newtonian Powell-Eyring model (P-EM) fluid is a constitutive equation employed for the characterization of the transient flow performance of non-Newtonian fluid, in which the viscosity depends on the rate of shear stress [34]. Several industrial and biological fluids like polymers, suspensions and biological fluids have more complicated flow behavior than Newtonian fluids and cannot be characterized by a simple Newtonian model [35]. In this respect, the P-EM is considered an improvement of the existing literature on fluid dynamics since it effectively combines both Newtonian and non-Newtonian performances of these materials [34]. P-EM is its potential for the prediction of liquid performance of shear rates. In contrast to other models, like Bingham plastic and power-law models, the present P-EM has no singularity at either high or low shear rates. The usage of the P-EM is suitable for utilization in a wide range of industries. In chemical engineering, it is applied in developing processes of polymer solutions, paints, and food products. However, in the field of biomedical, it contributes to the prediction of the flow characteristic of blood, which displays non-Newtonian properties that are essential to modeling circulation and designing products related to the circulatory system in the human body [36]. Also, the model is essential for the description of the flow of the drilling fluids and the crude oil, which can have rather complicated rheological behavior. The work of Hashim *et al.* [37] considers blood as a P-EM with hematocrit-dependent viscosity. They combined single-phase and two-phase mixture models to examine the thermal and mass transport properties of HNFs, highlighting the nominal toxicity and medicinal significance of ZnO–iron(III) oxide NPs. This exploration of thermal and mass transport phenomena in fluids with varying thermophysical features, focusing on P-EM with distinct characteristics, was studied [38]. However, they examine the performance of this shear-thinning fluid interacting with an exponentially stretchable surface, considering

influences such as thermal radiation. The effects of the radiation and thermal performance of a molybdenum disulfide and graphene oxide NPs on electromagnetic radiation absorption and enhanced thermal conductivity, driven by industrial demands for advanced non-Newtonian P-EM fluids were studied [39]. Entropy analysis of unsteady magnetohydrodynamic thin liquid film flow of Maxwell nanofluids with variable fluid properties was studied [40]. A renovated Jaffrey–Hamel flow problem and new scaling statistics for heat and mass fluxes with the Cattaneo–Christov heat flux model were studied [41]. Analytic solutions for a liquid film on an unsteady stretching surface were studied [42]. Heat transfer in a liquid film over an unsteady stretching surface with viscous dissipation in the presence of an external magnetic field was studied [43].

Fluid thin films are liquid layers with thicknesses ranging from nanometers to micrometers, exhibiting unique physical behaviors due to surface tension, viscosity, and external forces such as gravity, electromagnetic fields, and thermal gradients. These films play a critical role in numerous natural and industrial processes, influencing lubrication, coating technologies, biological systems, and heat transfer mechanisms. Fluid thin films have diverse applications in engineering and science. In coating and surface engineering, they are fundamental to processes such as painting, printing, and thin-film deposition in microelectronics. In thermal management systems, they enhance heat dissipation in cooling technologies, including microfluidic heat exchangers and phase-change materials. In biomedical applications, fluid thin films are crucial for drug delivery systems, tear film stability in ophthalmology, and bio-inspired microfluidics. Additionally, in aerospace and energy sectors, they are utilized in advanced lubrication systems, solar thermal energy collection, and fuel management in spacecraft. The study of fluid thin films continues to evolve with advancements in nanotechnology, smart coatings, and interfacial science, making them a key focus in modern applied physics, materials science, and engineering disciplines. Entropy generation and heat transfer in boundary layer flow over a thin needle moving in a parallel stream in the presence of nonlinear Rosseland radiation were studied by Afridi and Qasim [44]. Minimization of entropy generation in MHD mixed convection flow with energy dissipation and Joule heating: utilization of Sparrow–Quack–Boerner local non-similarity method was studied by Afridi *et al.* [45]. Comparative study and entropy generation analysis of Cu–H_2O and Ag–H_2O nanofluids flow over a slender stretching surface was studied by Afridi and Qasim [46]. Theoretical analysis of MHD Maxwell two-phase nano-flow subject to viscous dissipation and the chemical reaction was studied by Afridi *et al.* [47].

This study aims to investigate the enhancement of thermal transport and the effects of viscous dissipation in a time-dependent 2D thin liquid film composed of non-Newtonian HNF. The research focuses on the influence of solar radiation, Hall current, and second-order slip conditions on heat and mass transfer properties, with an emphasis on entropy generation and fluid transport efficiency. This study aims to formulate the governing equations for the time-dependent thin-film flow of a non-Newtonian HNF while incorporating the effects of solar radiation, Hall current, and second-order slip conditions. The HNF consists of magnesium oxide (MgO) and ZnO NPs suspended in water as the base fluid, ensuring enhanced thermal transport properties. The research seeks to transform these governing equations into a system of dimensionless ordinary differential equations (ODEs) using similarity variables to facilitate analysis. The study intends to solve the transformed ODEs numerically using the collocation method to obtain velocity, temperature, and entropy generation profiles. Additionally, it aims to analyze the influence of key physical parameters, such as the Brinkman number, magnetic field intensity, slip conditions, and solar radiation parameter, on the thermal and flow behavior of the HNF thin-film system. Furthermore, the research focuses on comparing the thermal transport performance and entropy production characteristics of the MgO–ZnO/water HNF with conventional nanofluids, emphasizing its advantages in improving heat transfer efficiency. Lastly, the study explores potential applications of the findings in biotechnology, medical therapies, and advanced energy storage systems, providing insights into optimizing thermal management in these fields.

2 Thermal fluid flow model description

Consider the transient, 2D motion of a non-Newtonian Powell-Eyring HNF, which exhibits both electrical conductivity and partial ionization, influenced by MHD effects and nanofluid interactions. The investigation incorporates thermal radiation and viscous dissipation phenomena over a dynamically extending sheet. A Cartesian coordinate framework ($\tilde{x}$, $\tilde{y}$), is employed, where the x-axis coincides with the stretching surface at $\tilde{y} = 0$, and the $\tilde{y}$-axis extends perpendicularly away from it. The sheet undergoes uniform elongation due to equal and opposite forces applied along the $\tilde{x}$-direction. To establish the governing equations, specific flow assumptions are introduced, as

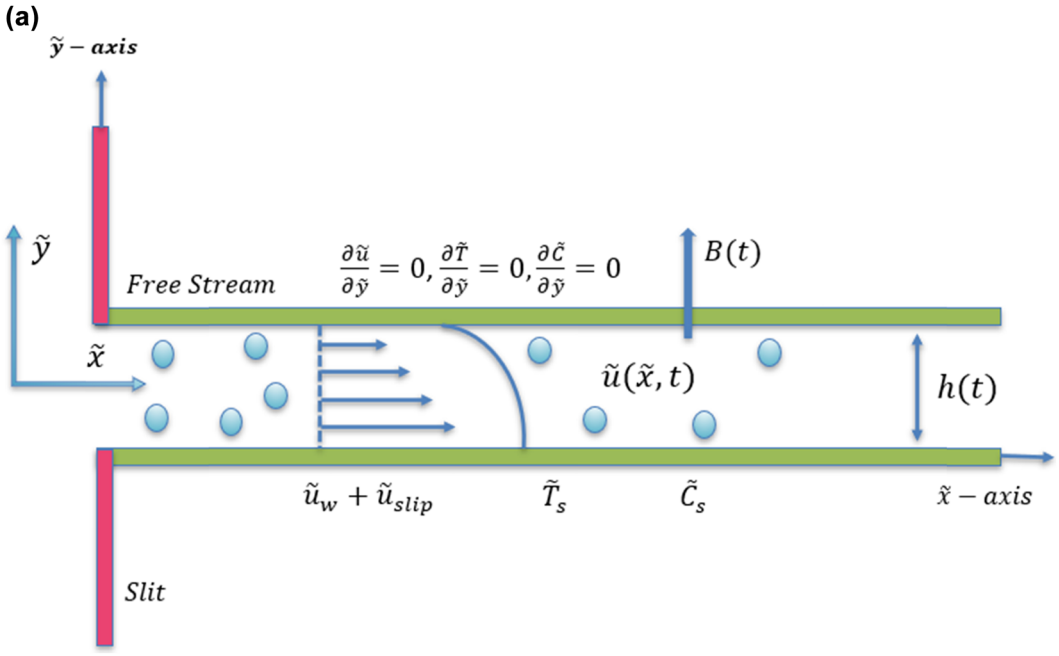

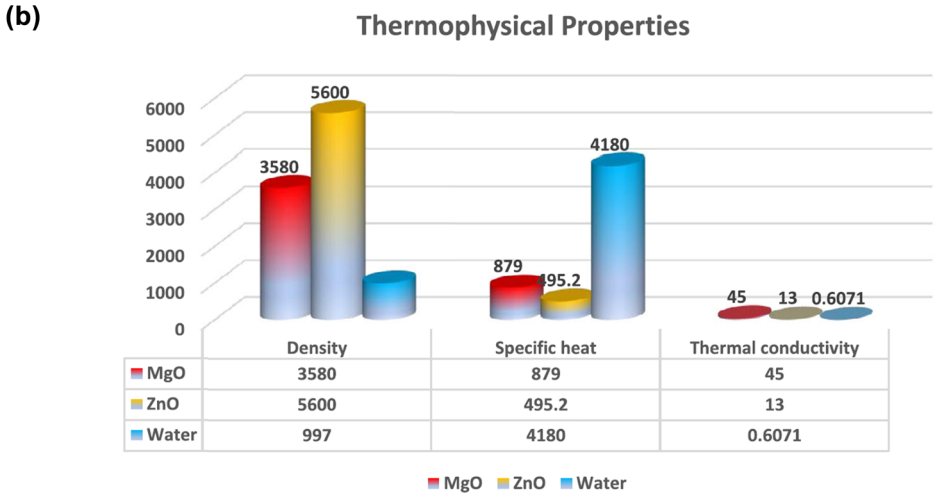

	Density	Specific heat	Thermal conductivity
MgO	3580	879	45
ZnO	5600	495.2	13
Water	997	4180	0.6071

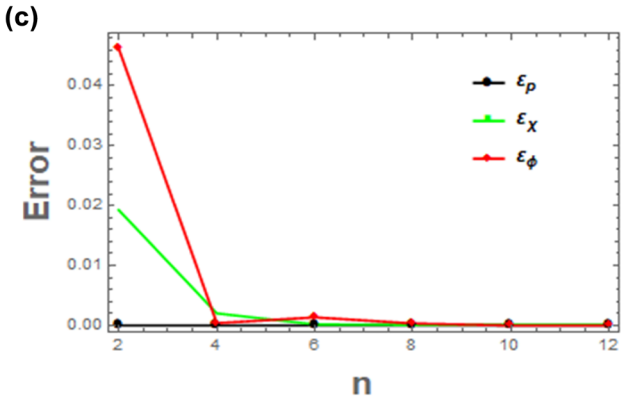

Figure 1: (a) Model configuration. (b) Thermophysical values for MgO, ZnO, and water-based fluid. (c) Minimized residual error.

shown in Figure 1a. The reference temperature and concentration are constrained by the conditions $0 \le \tilde{T}_{\text{ref}} \le \tilde{T}_0$ and $0 \le \tilde{C}_{\text{ref}} \le \tilde{C}_0$. The surface temperature is $\tilde{T}_{\text{s}}(\tilde{x}, t) = \tilde{T}_0 - \tilde{T}_{\text{ref}}\left(\frac{\mathrm{d}\tilde{x}^2}{2v_f}\right)\frac{1}{(1-at)^{1/2}}$ and concentration at the wall is $\tilde{C}_{\text{s}}(\tilde{x}, t) = \tilde{C}_0 - \tilde{C}_{\text{ref}}\left(\frac{\mathrm{d}\tilde{x}^2}{2v_{\text{f}}}\right)\frac{1}{(1-at)^{1/2}}$, where $\tilde{T}_{\text{s}}$ and $\tilde{C}_{\text{s}}$ represent the surface temperature and concentration, respectively. The fluid exhibits partial ionization, and external electromagnetic influences are neglected due to the dominance of inertial forces and negligible electric field effects. The thermal energy equation incorporates contributions from radiative heat transfer, Joule dissipation, viscous heating, spatially varying heat generation/absorption, and the influence of NP slip mechanisms. The nanofluid composition is analyzed using the Tiwari–Das model, which quantifies the volume fraction of MgO-ZnO NPs suspended in a water-based fluid, while the Buongiorno model accounts for the simultaneous impact of thermophoretic and Brownian diffusion. NPs are assumed to be uniformly distributed, maintaining thermal equilibrium with the surrounding base fluid. Both single-phase and two-phase formulations are considered, allowing for possible slip interactions between fluid molecules and suspended nanomaterials.

Following the highlighted assumptions, the governing boundary layer equations are described as [40,41]

Continuity equation

$$\nabla \cdot (\rho_{\text{unf}} V) = 0. \tag{1}$$

Momentum conservation equation

$$\left(\frac{\mathrm{d}V}{\mathrm{d}t}\right) = -\frac{1}{\rho_{\text{unf}}}\nabla p + \frac{1}{\rho_{\text{unf}}} J \times B + \frac{1}{\rho_{\text{unf}}}\nabla\cdot\tau. \tag{2}$$

Energy conservation equation

$$(\rho c_{\text{p}})_{\text{unf}}\left(\frac{\mathrm{d}\tilde{T}}{\mathrm{d}t}\right) = \nabla \cdot (k_{\text{unf}}\nabla\tilde{T}) - \nabla \cdot q_{\text{r}} + \text{tr}(\tau \cdot L) + (\rho c_{\text{p}})_{\text{P}}\left(D_{\text{B}}(\nabla\tilde{C} \cdot \nabla\tilde{T}) + \frac{D_{\text{T}}}{\tilde{T}_\infty}(\nabla\tilde{T})^2\right) + Q^* + \frac{1}{\sigma_{\text{f}}} J \cdot J. \tag{3}$$

Species concentration equation (mass transfer)

$$\left(\frac{\mathrm{d}\tilde{C}}{\mathrm{d}t}\right) = D_{\text{B}}\nabla^2\tilde{C} + \frac{D_{\text{T}}}{\tilde{T}_\infty}\nabla^2\tilde{T}. \tag{4}$$

Generalized Ohm's law:

$$\frac{\partial B}{\partial t} = \nabla \times E, \mu_0 J = \nabla \times B, \nabla \cdot B = 0,$$
$$J = \frac{\sigma_{\text{f}}}{1 + \left(\frac{\xi_{\varepsilon_i}}{U_e}\right)}\left((E + V \times B) - \frac{1}{e\xi_h} J \times B\right). \tag{5}$$

Table 1 displays the expressions of the above equation. The solar radiation (q_{r}) is given as

$$q_{\text{r}} = \left(-\frac{4\tilde{T}_0^3\sigma^*}{3k^*}\right)\frac{\partial}{\partial y}(\tilde{T}^4). \tag{6}$$

The non-uniform energy source expression is

$$Q^* = \frac{\tilde{u}_{\text{w}} k_{\text{f}}}{v_{\text{f}} x}(\mathscr{A}(\tilde{T}_{\text{s}} - \tilde{T}_0) + \mathscr{B}(\tilde{T} - \tilde{T}_0)). \tag{7}$$

Here, $\mathscr{A}$ represents the heat source, and $\mathscr{B}$ is the heat sink. The governing equations are described as

Table 1: Description and symbols

Expression/ term	Description	Symbol/meaning	Related context
ρ_{unf}, k_{unf}, $(\rho c_{\text{p}})_{\text{unf}}$, σ_{f}	Properties of the hybrid and base fluid: viscosity, thermal conductivity, heat capacitance, and electrical conductivity	ρ_{unf}: Viscosity, k_{unf}: Thermal conductivity, $(\rho c_{\text{p}})_{\text{unf}}$: Heat capacitance, σ_{f}: Electrical conductivity	These represent the fundamental properties of fluids involved in heat transfer and electrical conductivity
$\frac{\mathrm{d}}{\mathrm{d}t} = \frac{\mathrm{d}}{\mathrm{d}k^*} + (\cdot\nabla)^{*k}$	The convected derivative expression, combining time and spatial rate of change	$\mathrm{d}/\mathrm{d}t^*$: Total derivative, $\mathrm{d}/\mathrm{d}k^*$: Rate of change with respect to k, $(\cdot\nabla)$: Spatial derivative term	Describes the change of a quantity in both time and space (convection)
$J \times B$	Lorentz force due to the interaction between current density J and a uniform magnetic field B	J: Current density, B: Magnetic field	Represents the electromagnetic force on charged particles
$\frac{1}{e\xi_h}$	Hall expression, where ξ_h is related to electron number density, electron charge, and collision frequency	ξ_h: Hall term, e: electron charge, v_h: electron–atom collision frequency	Represents the effects of electromagnetic fields on electron and ion behavior, especially drift (Ion-slip)

$$\frac{\partial \tilde{u}}{\partial \tilde{x}} + \frac{\partial \tilde{v}}{\partial \tilde{y}} = 0, \tag{8}$$

$$\left(\frac{\partial \tilde{u}}{\partial t} + \tilde{u}\frac{\partial \tilde{u}}{\partial \tilde{x}} + \tilde{v}\frac{\partial \tilde{u}}{\partial \tilde{y}}\right) = \left(\frac{\mu_{\text{unf}}}{\rho_{\text{unf}}} + \frac{1}{\rho_{\text{unf}}\delta\varrho}\right)\frac{\partial^2 \tilde{u}}{\partial \tilde{y}^2} - \frac{\sigma_{\text{unf}}\tilde{B}_0^2\tilde{u}}{\rho_{\text{unf}}\sqrt{1-at}}\left(\frac{1+\xi_{\mathscr{H}}\xi_i}{(\xi_{\mathscr{H}})^2+(\xi_{\mathscr{H}}\xi_i)^2}\right) - \frac{1}{2\rho_{\text{unf}}\delta\varrho^3}\left(\frac{\partial \tilde{u}}{\partial \tilde{y}}\right)^2\frac{\partial^2 \tilde{u}}{\partial \tilde{y}^2}, \tag{9}$$

$$\begin{aligned}(\rho c_{\text{p}})_{\text{unf}}&\left(\frac{\partial \tilde{T}}{\partial t} + \tilde{u}\frac{\partial \tilde{T}}{\partial \tilde{x}} + \tilde{v}\frac{\partial \tilde{T}}{\partial \tilde{y}}\right)\\ &= \left(k_{\text{unf}} + \frac{16\sigma^*\tilde{T}_0^3}{3\kappa^*}\right)\frac{\partial^2 \tilde{T}}{\partial \tilde{y}^2} + \left(\mu_{\text{unf}} + \frac{1}{\delta\varrho}\right)\left(\frac{\partial \tilde{u}}{\partial \tilde{y}}\right)^2\\ &\quad - \frac{1}{2\beta\varrho^3}\left(\frac{\partial \tilde{u}}{\partial \tilde{y}}\right)^4 + (\rho c_{\text{p}})_{\text{p}}\left(D_{\text{B}}\left(\frac{\partial \tilde{C}}{\partial \tilde{y}}\right)\left(\frac{\partial \tilde{T}}{\partial \tilde{y}}\right) + \frac{D_{\text{T}}}{\tilde{T}_0}\left(\frac{\partial \tilde{T}}{\partial \tilde{y}}\right)^2\right) + \frac{\sigma_{\text{unf}}\tilde{B}_0^2u^2}{1-\text{at}}\left(\frac{1+\xi_{\mathscr{H}}\xi_i}{(\xi_{\mathscr{H}})^2+(\xi_{\mathscr{H}}\xi_i)^2}\right)\\ &\quad + \frac{\tilde{u}_w k_f}{v_f x}(\mathscr{A}(\tilde{T}_{\text{s}} - \tilde{T}_0) + \mathscr{B}(\tilde{T} - \tilde{T}_0)),\end{aligned} \tag{10}$$

$$\left(\frac{\partial \tilde{C}}{\partial t} + \tilde{u}\frac{\partial \tilde{C}}{\partial \tilde{x}} + \tilde{v}\frac{\partial \tilde{C}}{\partial \tilde{y}}\right) = D_{\text{B}}\left(\frac{\partial^2 \tilde{C}}{\partial \tilde{y}^2}\right) + \frac{D_{\text{T}}}{\tilde{T}_\infty}\frac{\partial^2 \tilde{T}}{\partial \tilde{y}^2}. \tag{11}$$

The boundary slip constraints are

$$\begin{aligned}\tilde{u} &= \tilde{u}_{\text{w}} + \tilde{u}_{\text{slip}} = \frac{\text{d}\tilde{x}}{1-at} + \frac{\forall}{\mu_{\text{f}}}\left(\left(\mu_{\text{hnf}} + \frac{1}{\delta\varrho}\right)\left(\frac{\partial \tilde{u}}{\partial \tilde{y}}\right) - \frac{1}{6\delta\varrho^3}\left(\frac{\partial \tilde{u}}{\partial \tilde{y}}\right)^3\right), \tilde{v} = 0,\\ \tilde{T} &= \tilde{T}_s, \tilde{C} = \tilde{C}_s : \tilde{y} \to 0,\end{aligned} \tag{12}$$

$$\frac{\partial \tilde{u}}{\partial \tilde{y}} = 0, \frac{\partial \tilde{T}}{\partial \tilde{y}} = 0, \frac{\partial \tilde{C}}{\partial \tilde{y}} = 0 \text{ and } \frac{\text{d}h}{\text{d}t} = 0 : \tilde{y} \to h. \tag{13}$$

Here, the velocity components in the $\tilde{x}$-direction ($\tilde{u}$) and in the y-direction ($\tilde{v}$), wall temperature ($\tilde{T}_{\text{s}}$), Hall parameter ($\xi_{\mathscr{H}}$), ion slip parameter (ξ_i), surface temperature, wall velocity ($\tilde{u}_{\text{w}}$), thermophoretic diffusion coefficient (D_{T}), temperature ($\tilde{T}$), second material parameter (ϱ), magnetic field strength ($\tilde{B}$), arbitrary constant (d, a), and the material parameter (δ). The thermophysical properties of nanofluid for μ_{unf}, ρ_{unf}, σ_{unf}, k_{unf}, and $(\rho C_{\text{p}})_{\text{unf}}$ are [45]

$$\rho_{\text{unf}} = (1-(\beta_1+\beta_2))\rho_{\text{f}} + \beta_1\rho_{s_1} + \beta_2\rho_{s_2},$$

$$\frac{k_{\text{unf}}}{k_{\text{nf}}} = \left(\frac{(k_{s2}+2k_{\text{nf}} - 2\beta_2(k_{\text{nf}} - k_{s2})}{(k_{s2}+2k_{\text{nf}} + \beta_2(k_{\text{nf}} - k_{s2})}\right),$$

$$\frac{k_{\text{nf}}}{k_{\text{f}}} = \left(\frac{k_{s1}+2k_{\text{f}} - 2\beta_1(k_{\text{f}} - k_{s1})}{(k_{s1}+2k_{\text{f}} + \beta_1(k_{\text{f}} - k_{s1})}\right),$$

$$\frac{\sigma_{\text{unf}}}{\sigma_{\text{f}}} = 1 + \frac{3\left(\frac{\beta_1\sigma_{s1}+\beta_2\sigma_{s2}}{\sigma_{\text{f}}} - (\beta_1+\beta_2)\right)}{\left(\frac{\beta_1\sigma_{s1}+\beta_2\sigma_{s2}}{(\phi_1+\phi_2)\sigma_{\text{f}}} + 2\right) - \left(\frac{\beta_1\sigma_{s1}+\beta_2\sigma_{s2}}{\sigma_{\text{f}}} - (\beta_1+\beta_2)\right)},$$

$$\mu_{\text{unf}} = \mu_{\text{f}}/(1-(\beta_1+\beta_2))^{2.5},$$

$$(\rho C_{\text{p}})_{\text{unf}} = (1-(\beta_1+\beta_2))(\rho C_{\text{p}})_{\text{f}} + \beta_1(\rho C_{\text{p}})_{s1} + \beta_2(\rho C_{\text{p}})_{s2}.$$

The thermophysical values for the MgO and ZnO NPs dispersed in a water-based fluid are displayed in Figure 1b.

The following transformations are [15,32,44]:

$$\begin{aligned}\psi &= \tilde{x}\sqrt{\frac{\text{d}v_f}{(1-at)}}p(\vartheta), \vartheta = y\sqrt{\frac{\text{d}}{v_{\text{f}}(1-at)}},\\ \epsilon &= \sqrt{\frac{\text{d}}{v_{\text{f}}(1-\tilde{a}t)}}h(t),\\ \chi(\vartheta) &= \frac{\tilde{T}-\tilde{T}_0}{\tilde{T}_s-\tilde{T}_0}, \phi(\vartheta) = \frac{\tilde{C}-\tilde{C}_0}{\tilde{C}_s-\tilde{C}_0},\\ \tilde{u} &= \frac{\partial \psi}{\partial \tilde{y}}, \tilde{v} = -\frac{\partial \psi}{\partial \tilde{x}}.\end{aligned} \tag{14}$$

Following the fulfillment of the mass conservation equation, the velocity components assume the following form:

$$\tilde{u} = \frac{\text{d}\tilde{x}}{(1-\tilde{a}t)}p'(\vartheta), \tilde{v} = -\sqrt{\frac{\text{d}v_f}{(1-\tilde{a}t)}}p(\vartheta), \tag{15}$$

where

$$\frac{\text{d}h}{\text{d}t} = -\frac{\epsilon d}{2}\sqrt{\frac{v_{\text{f}}}{a(1-at)}}. \tag{16}$$

We obtain

$$\begin{aligned}&(K_1+\varpi)p''(\vartheta) - \omega p''(\vartheta)p^2(\vartheta) + K_2\left(p(\vartheta)p'(\vartheta) - p^2(\vartheta) - S\left(p'(\vartheta) + \frac{\vartheta}{2}p'(\vartheta)\right)\right)\\ &- K_3\left(\frac{1+\xi_{\text{H}}\xi_{\text{i}}}{(\xi_{\text{H}})^2+(\xi_{\text{H}}\xi_{\text{i}})^2}\right)M_a p'(\vartheta) = 0,\end{aligned} \tag{17}$$

$$\begin{aligned}&\frac{1}{P_r}(K_5+N_{\text{r}})\chi'(\vartheta) + K_4\left(\frac{S}{2}(3\chi(\vartheta)+\vartheta\chi'(\vartheta)) + 2p'(\vartheta)\chi(\vartheta) - p(\vartheta)\chi'(\vartheta)\right)\\ &+ E_{\text{c}}\left((K_2+\varpi)p^2(\vartheta) - \frac{1}{3}\varpi\lambda p'^4(\vartheta)\right)\\ &+ K_3K_4E_{\text{c}}\left(\frac{1+\xi_h\xi_i}{(\xi_h)^2+(\xi_h\xi_i)^2}\right)M_a p^2(\vartheta) + N_{\text{b}}\chi'(\vartheta)\phi'(\vartheta)\\ &+ N_{\text{t}}\chi^2(\vartheta) + Ap'(\vartheta) + B\chi(\vartheta) = 0,\end{aligned} \tag{18}$$

$$\phi''(\vartheta) + S_c \left(p(\vartheta)\phi'(\vartheta) - 2p'^{(\vartheta)}\phi(\vartheta) - \frac{S}{2}(3\phi(\vartheta) + \vartheta\phi'(\vartheta))\right) + \frac{N_t}{N_b}\phi''(\vartheta) = 0, \tag{19}$$

Subject to:

$$p'(0) = 1 + N_1\left((K_2 + \varpi)p''(0) - \frac{1}{3}\varpi\omega(0)\right), \quad p(0) = 1, \chi(0) = 1, \phi(0) = 1. \tag{20}$$

The parameters associated with the velocity, temperature, and mass transfer rate are defined as follows:

$$\mathrm{Re}_x^{\frac{1}{2}}C_f = \left((K_2 + \varpi)(p'(0)) - \frac{1}{3}\varpi\omega(p'(0))^3\right), \quad Re_x^{-\frac{1}{2}}\mathrm{Nu}x = -(K_5 + \mathrm{Nr})\chi'(0), \quad \mathrm{Re}_x^{-\frac{1}{2}}\mathrm{Sh}x = \phi'(0), \tag{21}$$

Here, viscoelastic is $\omega = \frac{\tilde{u}_w^2 d}{2\nu_f \gamma'}$, solar radiation $\mathrm{Nr} = \frac{16\sigma^*\tilde{T}_0^3}{3\kappa^* k_f}$, Brownian motion $N_b = \frac{\tau_1 D_B(\tilde{C}_s - \tilde{C}_0)}{\nu_f}$, thermophoresis $N_t = \frac{\tau_1 D_T(\tilde{T}_s - \tilde{T}_0)}{\nu_f \tilde{T}_\infty}$, viscosity is $\varpi = \frac{1}{\delta\varrho\mu_f}$, magnetic $M_a = \frac{\sigma_f B_0^2}{\rho_f d}$, concentration difference $E_2 = \frac{(\tilde{C}_s - \tilde{C}_0)}{\tilde{C}_0}$, Eckert $\mathrm{Ec} = \frac{\mu_w^2}{(\rho c_p)_f(\tilde{T}_s - \tilde{T}_0)}$, slip $N_1 = \mathcal{O}\sqrt{\frac{a}{\nu_f}}$, Schmidt $\mathrm{Sc} = \frac{\nu_f}{D_B}$, Prandtl $\mathrm{Pr} = \frac{(\mu c_p)_f}{k_f}$, temperature difference $D_1 = \frac{(\tilde{T}_s - \tilde{T}_0)}{T_0}$, unsteadiness $S = \frac{d}{a}$, diffusion $\chi_1 = \frac{\mathrm{RD}_B(\tilde{C}_s - \tilde{C}_0)}{k_f}$.

3 Entropy production analysis

The entropy generation is presented by

$$G_s = \frac{1}{\tilde{T}_0^2}\left(k_{unf} + \frac{16\sigma^*\tilde{T}_0^3}{3\kappa^*}\right)\left(\frac{\partial\tilde{T}}{\partial\tilde{y}}\right)^2 + \frac{1}{\tilde{T}_0}\left[\left(\mu_{unf} + \frac{1}{\delta\varrho}\right)\left(\frac{\partial\tilde{u}}{\partial\tilde{y}}\right)^2 - \frac{1}{2\beta\varrho^3}\left(\frac{\partial\tilde{u}}{\partial\tilde{y}}\right)^4\right] + \left(\frac{\mathrm{RD}_T}{\tilde{T}_0}\left(\frac{\partial\tilde{C}}{\partial\tilde{y}}\right)\left(\frac{\partial\tilde{T}}{\partial\tilde{y}}\right) + \frac{\mathrm{RD}_B}{\tilde{C}_0}\left(\frac{\partial\tilde{C}}{\partial\tilde{y}}\right)^2\right) + \frac{\sigma_{unf}B_0^2\tilde{u}^2}{\tilde{T}_0(1 - at)}\left(\frac{1 + \xi_H\xi_i}{(\xi_H)^2 + (\xi_H\xi_i)^2}\right), \tag{22}$$

The dimensionless entropy production is

$$\mathrm{MG} = \frac{\tilde{T}_0^2(\vartheta/\tilde{y})^2}{k_f(\tilde{T}_s - \tilde{T}_0)}G_s, \tag{23}$$

$$\mathrm{MG} = (K_5 + N_r)\chi'^2(\vartheta) + \frac{B_r}{E_1}\left((K_2 + \varpi)p'^2(\vartheta) - \frac{1}{3}\varpi\omega p'^4(\vartheta)\right) + \varsigma_1\frac{E_2}{E_1}\phi^2 + D_1\phi'\chi' + \frac{K_3 M_a B_r}{E_1}\left(\frac{1 + \delta_H\delta_i}{(\delta_H)^2 + (\delta_H\delta_i)^2}\right)p'^2, \tag{24}$$

$$\mathrm{MG} = M_{G,H} + M_{G,F} + M_{G,J} + M_{G,M}. \tag{25}$$

4 Numerical solution

4.1 The application of the collocation-weighted residual

The collocation-weighted residual method is applied to solve the governing Eqs. (17)–(19) with the boundary conditions in Eq. (20). Approximate solution is obtained as

$$p(\vartheta) \approx \sum_{j=1}^{n} c_j\Phi_j(\vartheta), (\vartheta) \approx \sum_{j=1}^{n} d_j\Phi_j(\vartheta), \ \phi(\vartheta) \approx \sum_{j=1}^{n} e_j\Phi_j(\vartheta). \tag{26}$$

Here, $\Phi_j(\vartheta)$ are the basis functions and c_j, d_j, e_j are coefficients to be determined.

Substitute the approximations for $p(\vartheta), p'(\vartheta)$, and $p''(\vartheta)$ into the differential equations

$$p(\vartheta) \approx \sum_{j=1}^{n} c_j\Phi_j(\vartheta), \quad p'(\vartheta) \approx \sum_{j=1}^{n} c_j\Phi_j'(\vartheta), \quad p''(\vartheta) \approx \sum_{j=1}^{n} c_j\Phi_j''(\vartheta), \tag{27}$$

$$(\vartheta) \approx \sum_{j=1}^{n} d_j\Phi_j(\vartheta), \quad \chi'(\vartheta) \approx \sum_{j=1}^{n} d_j\Phi_j'(\vartheta), \quad \chi''(\vartheta) \approx \sum_{j=1}^{n} d_j\Phi_j''(\vartheta), \tag{28}$$

$$\phi(\vartheta) \approx \sum_{j=1}^{n} e_j\Phi_j(\vartheta), \quad \phi'(\vartheta) \approx \sum_{j=1}^{n} e_j\Phi_j'(\vartheta), \quad \phi''(\vartheta) \approx \sum_{j=1}^{n} e_j\Phi_j''(\vartheta). \tag{29}$$

Expand $p^2(\vartheta)$, $p^2(\vartheta)$ and $p^4(\vartheta)$ as

$$p^2(\vartheta) \approx \left(\sum_{j=1}^{n} c_j\Phi_j(\vartheta)\right)^2, p'^4(\vartheta) \approx \left(\sum_{j=1}^{n} c_j\Phi_j'(\vartheta)\right)^4. \tag{30}$$

Expand the nonlinear term $p''(\vartheta)p^2(\vartheta)$

$$p''(\vartheta)p^2(\vartheta) \approx \left(\sum_{j=1}^{n} c_j\Phi_j''(\vartheta)\right)\left(\sum_{k=1}^{n} c_k\Phi_k(\vartheta)\right)^2, \tag{31}$$

$$\begin{aligned}(\vartheta) &\approx \sum_{j=1}^{n} d_j\Phi_j(\vartheta), \quad \chi'(\vartheta) \approx \sum_{j=1}^{n} d_j\Phi_j'(\vartheta),\\ \chi''(\vartheta) &\approx \sum_{j=1}^{n} d_j\Phi_j''(\vartheta).\end{aligned} \tag{32}$$

Substitute into the momentum equation at collocation points ϑ_i:

$$\begin{aligned}&(K_1+\omega)\sum_{j=1}^{n} c_j\Phi_j''(\vartheta_i) - \lambda\omega\left(\sum_{j=1}^{n} c_j\Phi_j''(\vartheta_i)\right)\left(\sum_{j=1}^{n} c_j\Phi_j(\vartheta_i)\right)^2\\ &\quad + K_2\left(\left(\sum_{j=1}^{n} c_j\Phi_j(\vartheta_i)\right)\left(\sum_{j=1}^{n} c_j\Phi_j'(\vartheta_i)\right) - \left(\sum_{j=1}^{n} c_j\Phi_j(\vartheta_i)\right)^2\right.\\ &\quad \left. - S\left(\sum_{j=1}^{n} c_j\Phi_j'(\vartheta_i) + \frac{\vartheta_i}{2}\sum_{j=1}^{n} c_j\Phi_j'(\vartheta_i)\right)\right)\\ &\quad - K_3\frac{(1+\xi_H\xi_i)}{\xi_H^2 + (\xi_H\xi_i)^2}M_a\sum_{j=1}^{n} c_j\Phi_j'(\vartheta_i) = 0.\end{aligned} \tag{33}$$

$$\begin{aligned}&\frac{1}{P_r}(K_5+N_r)\sum_{j=1}^{n} d_j\Phi_j'(\vartheta_i) + K_4\left(\frac{S}{2}\left(3\sum_{j=1}^{n} d_j\Phi_j(\vartheta_i)\right.\right.\\ &\quad \left. + \vartheta_i\sum_{j=1}^{n} d_j\Phi_j'(\vartheta_i)\right) + 2\left(\sum_{j=1}^{n} c_j\Phi_j'(\vartheta_i)\right)\left(\sum_{j=1}^{n} d_j\Phi_j(\vartheta_i)\right)\\ &\quad \left. - \left(\sum_{j=1}^{n} c_j\Phi_j(\vartheta_i)\right)\left(\sum_{j=1}^{n} d_j\Phi_j'(\vartheta_i)\right)\right)\\ &\quad + E_c\left((K_2+\omega)\left(\sum_{j=1}^{n} c_j\Phi_j(\vartheta_i)\right)^2 - \frac{\omega\lambda}{3}\left(\sum_{j=1}^{n} c_j\Phi_j'(\vartheta_i)\right)^4\right)\\ &\quad + K_3K_4E_c\frac{(1+\xi_H\xi_i)}{\xi_H^2 + (\xi_H\xi_i)^2}M_a\left(\sum_{j=1}^{n} c_j\Phi_j(\vartheta_i)\right)^2\\ &\quad + N_b\left(\sum_{j=1}^{n} d_j\Phi_j'(\vartheta_i)\right)\left(\sum_{j=1}^{n} e_j\Phi_j'(\vartheta_i)\right) + N_t\left(\sum_{j=1}^{n} d_j\Phi_j(\vartheta_i)\right)^2\\ &\quad + A\left(\sum_{j=1}^{n} c_j\Phi_j'(\vartheta_i)\right) + B\left(\sum_{j=1}^{n} d_j\Phi_j(\vartheta_i)\right) = 0,\end{aligned} \tag{34}$$

$$\begin{aligned}&\sum_{j=1}^{n} e_j\Phi_j'(\vartheta) + S_c\left(\left(\sum_{j=1}^{n} c_j\Phi_j(\vartheta)\right)\left(\sum_{j=1}^{n} e_j\Phi_j'(\vartheta)\right)\right.\\ &\quad - 2\left(\sum_{j=1}^{n} c_j\Phi_j'(\vartheta)\right)\left(\sum_{j=1}^{n} e_j\Phi_j(\vartheta)\right) - \frac{S}{2}\left(3\sum_{j=1}^{n} e_j\Phi_j(\vartheta)\right.\\ &\quad \left.\left. + \vartheta\sum_{j=1}^{n} e_j\Phi_j'(\vartheta)\right)\right) + \frac{N_t}{N_b}\sum_{j=1}^{n} e_j\Phi_j'(\vartheta) = 0.\end{aligned} \tag{35}$$

Subject to

$$\begin{aligned}p(0) &= \sum_{j=1}^{n} c_j\Phi_j(0) = 1, \phi(0) = \sum_{j=1}^{n} e_j\Phi_j(0) = 1,\\ p'(0) &= \sum_{j=1}^{n} c_j\Phi_j'(0) = 1 + N_1\left[(K_2+\omega)\sum_{j=1}^{n} c_j\Phi_j''(0)\right.\\ &\quad \left. - \frac{\omega\lambda}{3}\left(\sum_{j=1}^{n} c_j\Phi_j'(0)\right)^3\right].\end{aligned} \tag{36}$$

Figure 1c displays the minimized residual error achieved using Mathematica software. Table 2 demonstrates that the results from the present model closely agree with the findings reported in refs. [42–44] for $\mathrm{Re}_x^{\frac{1}{2}}C_f$ across different values of the S parameters.

5 Graphical interpretation of the results

The phenomenon of slip mechanism in the flow characteristics of magnesium and ZnO water-based fluids within the thin film flow of partially ionized Powell-Eyring fluid under solar radiation is examined in this study. The results obtained using the collocation method with the assistance of Wolfram Mathematica software are presented in this section. The graphical representations illustrate the fluid velocity, temperature, and mass profiles, while the corresponding physical and engineering parameters are systematically summarized in tabular form. From Table 1, as material parameters (ϖ) upsurges from 0.5 to 0.7, the heat transfer rate ($\mathrm{Re}_x^{-\frac{1}{2}}\mathrm{Nu}x$) generally increases from 0.1328 to 0.2206. Growing material parameters (ω) from 0.5 to 0.7 results in greater $\mathrm{Re}_x^{-\frac{1}{2}}\mathrm{Nu}x$. An increase in Brownian diffusion parameter and thermophoresis diffusion parameter tends to promote the ($\mathrm{Re}_x^{-\frac{1}{2}}\mathrm{Nu}x$). Greater values of Eckert number show more noticeable viscous dissipation impact, contributing to superior heat transfer rate values. Both the Hall parameter and ion slip parameter appear to stabilize ($\mathrm{Re}_x^{-\frac{1}{2}}\mathrm{Nu}x$) (Table 3).

Magnetic field (M_a) parameter: Figure 2a presents a graph illustrating the variation of $p'(\vartheta)$ against ϑ for different values of the magnetic parameter M_a. The graph contains three distinct curves corresponding to different values of the magnetic parameter, where the red curve represents M_a = 0.2. The blue curve represents M_a = 0.4. The black dashed curve represents M_a = 0.6. From the figure, it is evident that $p'(\vartheta)$ decreases as ϑ increases. Additionally, as the magnetic parameter M_a increases, the values of $p'(\vartheta)$ decrease more rapidly. The downward

Table 2: Numerical values of $\mathrm{Re}_x^{\frac{1}{2}} C_f$

$\mathrm{Re}_x^{\frac{1}{2}} C_f$ S	1.0	1.2	1.4	1.6
Result of [42]	2.677222162	2.677222162	1.999591426	1.447754361
Result of [43]	2.6772221621	2.6772221621	1.9995914260	1.4477543611
Result of [44]	2.6778	2.6778	1.9998	1.4479
Current findings	2.6772221621	2.6772221621	1.9995914260	1.4477543611

arrow in the graph further emphasizes this trend, indicating that a stronger magnetic field leads to a more significant reduction in $p'(\vartheta)$. In the context of MHD, an increase in the magnetic parameter introduces a stronger Lorentz force, which acts as a resistive force opposing the motion of the fluid. The observed trend in the figure aligns with this theoretical expectation, as higher values of M_a correspond to lower value $p'(\vartheta)$, indicating that the applied magnetic field increases resistance within the fluid flow. Additionally, the smooth and monotonic decrease in $p'(\vartheta)$ suggests that the presence of the magnetic field enhances dissipation effects, causing the gradient to diminish more rapidly. This behavior is commonly observed in MHD flow problems, where the presence of a magnetic field reduces the overall kinetic energy of the fluid. This phenomenon has important implications in engineering and industrial applications, including MHD generators and pumps, thermal control in nuclear reactors, and aerospace and industrial applications. In Figure 2b, the $\chi(\vartheta)$ illustrates its behavior as the value of M_a increases. The parameter M_a influences the fluid temperature, and it is evident from the curves in Figure 2b that higher values of M_a lead to an increase in $\chi(\vartheta)$.

Table 3: Calculation for Nusselt number

ϖ	ω	Ec	N_b	N_t	N_r	ξ_h	ξ_i	A	Nux
0.5	0.5	0.4	0.2	0.2	0.6	0.1	0.5	6	2.1580
0.6	0.5	0.4	0.2	0.2	0.6	0.1	0.5	6	2.1802
0.7	0.5	0.4	0.2	0.2	0.6	0.1	0.5	6	2.1995
0.5	0.3	0.4	0.2	0.2	0.6	0.1	0.5	6	2.2120
	0.4	0.4	0.2	0.2	0.6	0.1	0.5	6	2.2315
	0.5	0.4	0.2	0.2	0.6	0.1	0.5	6	2.2498
0.5	0.5	0.4	0.2	0.2	0.6	0.1	0.5	6	2.2120
	0.5	0.5	0.2	0.2	0.6	0.1	0.5	6	2.2315
	0.5	0.6	0.2	0.2	0.6	0.1	0.5	6	2.2498
0.5	0.5	0.4	0.2	0.2	0.6	0.1	0.5	6	2.2051
	0.5	0.4	0.4	0.2	0.6	0.1	0.5	6	2.2298
	0.5	0.4	0.6	0.2	0.6	0.1	0.5	6	2.2534
0.5	0.5	0.4	0.2	0.2	0.6	0.1	0.5	6	2.2002
	0.5	0.4	0.2	0.4	0.6	0.1	0.5	6	2.2267
	0.5	0.4	0.2	0.6	0.6	0.1	0.5	6	2.2501
0.5	0.5	0.4	0.2	0.2	0.6	0.1	0.5	6	2.2202
	0.5	0.4	0.2	0.2	0.7	0.1	0.5	6	2.2486
	0.5	0.4	0.2	0.2	0.8	0.1	0.5	6	2.2486
0.5	0.5	0.4	0.2	0.2	0.6	0.1	0.5	6	2.2234
	0.5	0.4	0.2	0.2	0.6	0.1	0.5	6	2.2521
	0.5	0.4	0.2	0.2	0.6	0.5	0.5	6	2.2807
0.5	0.5	0.4	0.2	0.2	0.6	0.9	0.5	6	2.5353
	0.5	0.4	0.2	0.2	0.6	0.1	0.5	6	2.7526
	0.5	0.4	0.2	0.2	0.6	0.1	0.6	6	2.8563
0.5	0.5	0.4	0.2	0.2	0.6	0.1	0.7	6	2.4372
	0.5	0.4	0.2	0.2	0.6	0.1	0.5	6	2.8923
	0.5	0.4	0.2	0.2	0.6	0.1	0.5	7	2.9421

Material parameters (ϖ, ω): Figure 2c and d show the impact of Eyring–Powell first and second parameter $p'(\vartheta)$. The influence of the ϖ parameter on the $p'(\vartheta)$ is shown in Figure 2c. As ϖ upsurges, the flow impedance reduces. From a physical perspective, an increase in the viscosity parameter corresponds to a decrease in fluid molecular viscosity. This reduction in viscosity leads to a decline in the nanofluid velocity and a suppression of the boundary layers. Figure 2d plot displays the influence of the Eyring–Powell second parameter (ω), which upsurges for the values of 2, 4, and 6. Unlike Eyring–Powell first parameter, $p'(\vartheta)$ upsurges as ω rises. This performance is the result of the elastic nature of the material that enables stress-free flow. More specifically, it was observed that the Eyring–Powell second parameter (ω) improved the capacity of the material to deform and align in the wall under shear pressures, which in turn reduces the internal resistance to flow. Physically, it can be associated with polymeric or viscoelastic fluids, for example, in some production processes, molten plastics or polymer solutions, where the flow of the liquid under stress becomes more streamlined. In general, for such material, more excellent elasticity or deformability increases flow effectiveness, as has been illustrated *via* the growing $p'(\vartheta)$.

Figure 3a illustrates the variation of $p'(\vartheta)$ with respect to ϑ, where different curves represent varying values of the Hall parameter (ξ_h) and the ion slip parameter (ξ_i). The red curve corresponds to ξ_h, ξ_i = 4, the blue curve represents ξ_h, ξ_i = 5, and the black dashed curve signifies ξ_h, ξ_i = 6. As ϑ increases along the horizontal axis, the values of $p'(\vartheta)$ decrease for all cases. However, an increase in ξ_h and ξ_h shifts the curves upward, indicating that higher values of

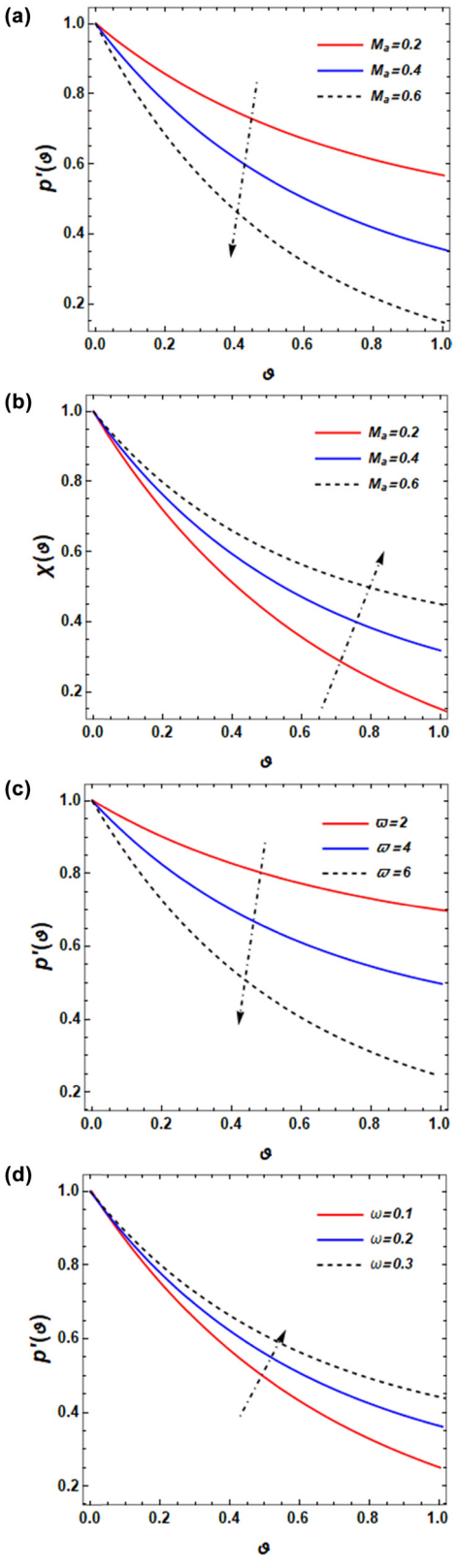

Figure 2: (a) Effect of M_a on $p'(\vartheta)$. (b) Influence of M_a on $\chi(\vartheta)$. (c) Effect of ϖ on $p'(\vartheta)$. (d) Influence of ω on $p'(\vartheta)$.

these parameters lead to an overall increase in $p'(\vartheta)$. The arrow in the figure emphasizes the direction of this trend, highlighting the progressive rise in $p'(\vartheta)$ with increasing ξ_h and ξ_i. The $\chi(\vartheta)$ is influenced by the ξ_h and ξ_i parameters as revealed in Figure 3b. Greater values of ξ_h and ξ_i upsurge the $\chi(\vartheta)$. The upward shift of the curves with increasing ξ_h and ξ_i indicates that larger values of these parameters enhance the function $\chi(\vartheta)$. The arrow in the figure marks the trend direction, demonstrating the progressive increase of $\chi(\vartheta)$ as the Hall and ion slip parameters grow. This trend suggests that the Hall and ion slip effects play a crucial role in modifying $\chi(\vartheta)$, ultimately impacting the transport and flow characteristics within the system. From a practical perspective, these findings have direct applications in various engineering and industrial systems. In plasma physics, the Hall and ion slip effects are essential in controlling plasma flow in fusion reactors and space propulsion technologies. In semiconductor processing, these parameters influence the behavior of ionized gases used in thin-film deposition and microelectronics manufacturing. Additionally, in energy systems such as MHD

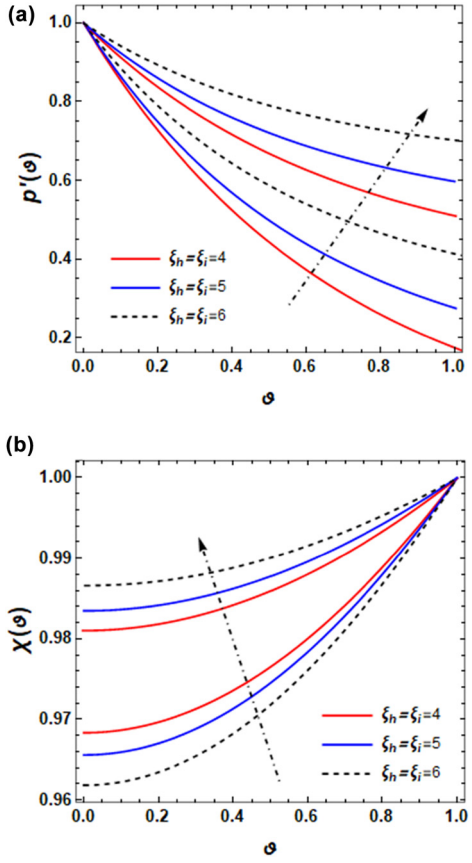

Figure 3: (a) Effect of ξ_h and ξ_i on $p'(\vartheta)$. (b) Influence of ξ_h and ξ_i on $\chi(\vartheta)$.

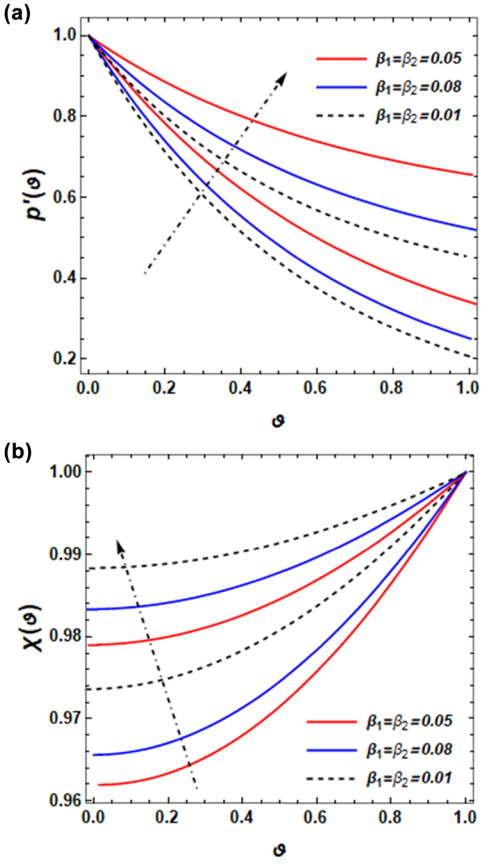

Figure 4: (a) Effect of β_1, β_2 on $p'(\vartheta)$. (b) Influence of β_1, β_2 on $\chi(\vartheta)$.

power generators and liquid metal cooling in nuclear reactors, optimizing the Hall and ion slip effects can enhance efficiency by regulating flow stability and heat transfer characteristics. The observed trends can also be applied in biomedical applications, particularly in the design of magnetic drug targeting and blood flow regulation under electromagnetic influences.

Figure 4a and b illustrates the impact of the NP volumetric fraction ($\beta_1 = \beta_2$) on both velocity and temperature profiles in a nanofluid system. The volumetric fraction of NPs is a critical parameter in nanofluid dynamics as it influences the transport properties, such as thermal conductivity and viscosity, which subsequently affect fluid motion and heat transfer efficiency. An increase in $\beta_1 = \beta_2$ modifies the velocity distribution by altering the momentum diffusion and fluid resistance. Since NPs enhance the effective viscosity and density of the fluid, they tend to influence the overall flow behavior, leading to either an increase or decrease in velocity. Additionally, the temperature distribution is significantly affected as the presence of a higher NP fraction enhances thermal

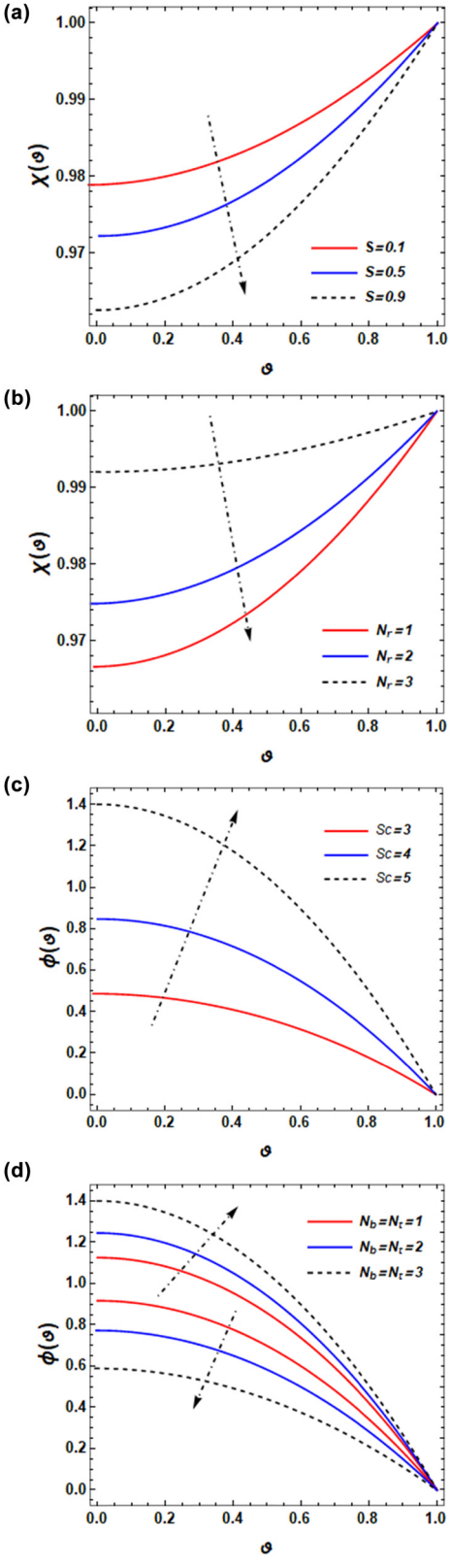

Figure 5: (a) Influence of S on $\chi(\vartheta)$. (b) Influence of N_r on $\chi(\vartheta)$. (c) Influence of Sc on $\phi(\vartheta)$. (d) Influence of $N_t = N_b$ on $\phi(\vartheta)$.

conductivity, thereby improving heat transport within the fluid. The resulting thermal enhancement is particularly beneficial in applications requiring efficient energy transport, such as solar thermal systems, electronic cooling, and biomedical heat exchangers. These findings are particularly relevant in engineering applications where precise control over velocity and temperature fields is required. The optimization of NP concentrations can lead to improvements in industrial cooling, aerospace thermal management, and advanced manufacturing processes where heat dissipation plays a critical role in system performance. Furthermore, in medical applications such as hyperthermia treatment and targeted drug delivery, understanding the role of NP fractions aids in improving the efficiency of thermal therapy and the transport of therapeutic agents within biological fluids.

Unsteadiness parameter (S): The unsteadiness parameter is generally characterized as the relative rates of time dependence to a steady state within the governing equations for energy transfer. From Figure 5a, it can be shown that the influence S decreases the $\chi(\vartheta)$ throughout the thermal boundary layer. This implies that the heat retention of the fluid decreases as the system changes. Therefore, when the system is less stable, it takes a relatively small amount of time for a given fluid particle. The S plays an important function in determining the $\chi(\vartheta)$ within a thermal boundary layer. As the unsteadiness parameter upsurges, the $\chi(\vartheta)$ declines, as a result, of decreased heat retention.

Solar radiation parameter (N_r): The radiation parameter (N_r) describes the impact of solar radiation on fluid systems. Figure 5b shows that with the gradual rise in the radiation parameter, the $\chi(\vartheta)$ also increases. This means that high solar radiation leads to a higher temperature system. Physically, due to higher solar radiation, the densities of irradiative heat transfer also rise and enhance the thermal energy transfer rate in the medium. Higher

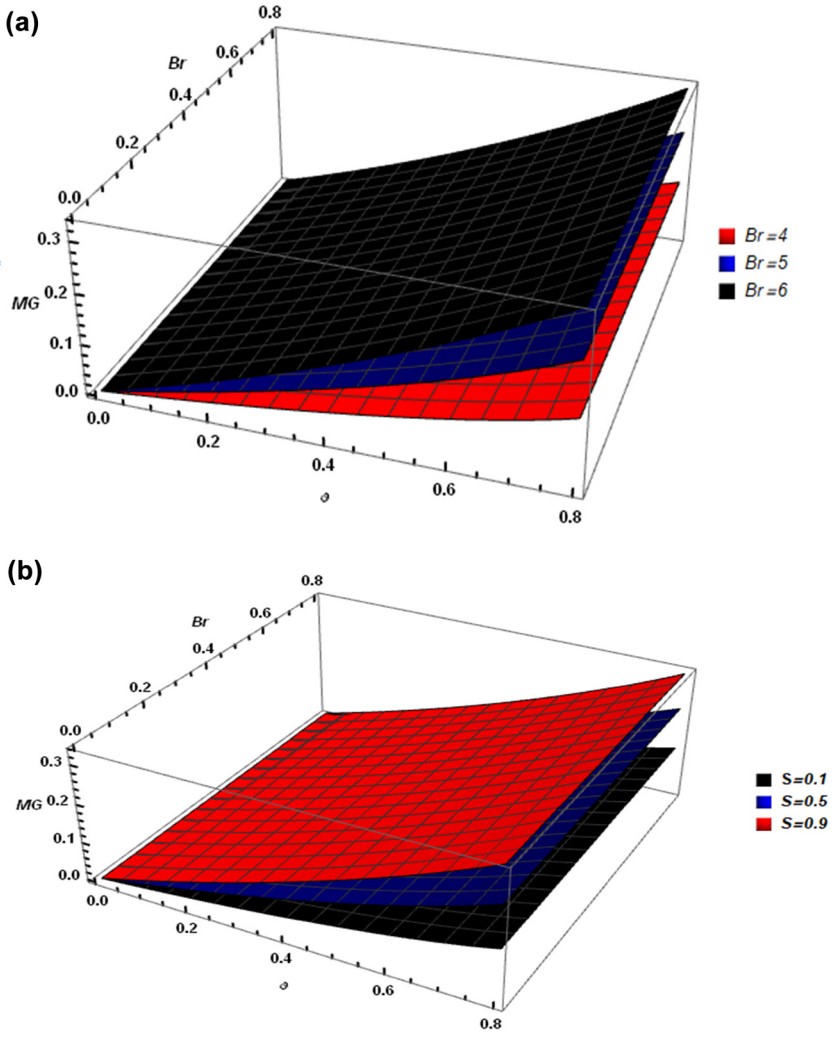

Figure 6: (a) 3D plot showing the influence of Br on entropy production. (b) 3D plot showing the influence of S on entropy production.

density of solar radiation brings extra thermal energy that increases the fluid temperature. Improved N_r offers more energy to the system, which is immersed *via* the medium, leading to an overall intensification in temperature.

Schmidt number (Sc): Schmidt number (Sc) is a non-dimensional quantity that relates the ratio of momentum diffusivity to mass diffusivity within a fluid system. The greater value of Sc displays that momentum diffuses faster than mass, and the thickness of the mass boundary layer is much smaller than the velocity boundary layer. Figure 5c demonstrates the mass profile $\phi(\vartheta)$ for various values of the Sc. As the Sc upsurges, the $\phi(\vartheta)$ declines throughout the boundary layer. This shows that larger Sc values influence in lower concentrations of the solute at all points within the liquid. With a greater value of the Schmidt number, the thickness of the concentration boundary layer diminishes.

The variation of the thermophoresis parameter and Brownian motion parameter concerning the nanofluid concentration is analyzed in Figure 5d, emphasizing their respective performances across different concentration levels. The figure exemplifies how the concentration displays both growing and reducing trends in response to variations in thermophoresis parameter and Brownian motion. The outcomes suggest that a greater value (N_t) significantly influences and improves the upsurge in nanofluid concentration. The $\phi(\vartheta)$ declines across the concentration's boundary layer. This reduction happens because thermophoresis drives particles away from high-temperature regions close to the surface. This movement of particles lowers their concentration within the boundary layer, thereby decreasing the $\phi(\vartheta)$. It is revealed that the concentration boundary layer reduces as the Brownian motion declines. A rise in the N_b increases the mobility of NPs. The effect of the Brinkman number (B_r) on the entropy generation profile is seen in Figure 6a. The Br signifies the ratio of energy produced through viscous dissipation to the energy transported through molecular conduction. In reality, an increase in the Brinkman number shows an improvement in heat production due to viscous dissipation, leading to a raised entropy production rate. Also, Figure 6b displays the 3D plot of the S parameter. It is observed that the entropy production rate decreases with higher values of the S parameter.

6 Conclusion

This study investigated the dissipative disorder optimization in the radiative thin film flow of a partially ionized non-Newtonian HNF (MgO + ZnO~water base fluid) under a second-order slip condition. The analysis considered the combined effects of thermal radiation, magnetic field, and viscous dissipation on heat and mass transfer dynamics. The inclusion of MgO and ZnO NPs significantly enhanced the thermal conductivity and energy transport efficiency of the fluid, leading to improved heat dissipation and fluid stability. Moreover, the second-order slip condition played a crucial role in modulating velocity and temperature distributions, which directly affected thin film stability and boundary layer behavior. Additionally, the interplay between ionization effects and dissipative mechanisms influenced entropy generation, which is critical for optimizing energy utilization in thermal systems. These findings provide valuable insights into improving heat management strategies in industrial applications such as cooling technologies, thin film coatings, and microfluidic systems. The findings highlight significant observations arising from the variation of these factors, which are as follows:

- An increase in material parameters, Brownian motion, and thermophoretic diffusion enhances the rate of energy transport, promoting improved heat distribution within the fluid.
- The thermal performance of the fluid improved as both the intensity of solar radiation and the NP volume fraction increased, leading to a significant rise in heat absorption and energy transport efficiency.
- The magnetic parameter significantly influences the progression of film thickness, governing its evolution over time.
- A higher magnetic parameter and NP volume fraction contribute to a decrease in velocity profiles, demonstrating increased flow suppression.
- An increase in the Eckert number amplifies the impact of viscous dissipation, enhancing thermal energy generation within the fluid.
- The Hall parameter and ion slip parameter significantly affect the heat transfer rate, characterized by $\mathrm{Re}_x^{-\frac{1}{2}}\mathrm{Nu}x$, leading to notable variations in thermal performance.
- Rising Brinkman number trends impact entropy generation, with the MgO + ZnO ~ water base fluid exhibiting superior efficiency in enhancing entropy production.

7 Future study

Based on the findings of this study on thermal transport and viscous dissipation in a time-dependent 2D thin liquid film of non-Newtonian HNFs, several future research directions can be explored to further enhance understanding and practical applications: Investigate the behavior of HNFs in 3D thin film flows to capture more realistic fluid dynamics. Analyze the effects of curved and irregular

surfaces, such as rotating disks, cones, and porous substrates, to mimic real-world engineering applications. Consider the temperature-dependent viscosity, thermal conductivity, and density of HNFs for a more precise representation of real fluids. Study the impact of NP shape factors (spherical, cylindrical, platelet, *etc.*) on thermal transport and viscous dissipation. By addressing these areas, future studies can enhance the applicability of HNFs in energy systems, aerospace, biomedical engineering, and industrial heat transfer technologies.

Acknowledgments: The authors extend their appreciation for the support of Princess Nourah bint Abdulrahman University Researchers Supporting Project number (PNURSP2025R163), Princess Nourah bint Abdulrahman University, Riyadh, Saudi Arabia. In addition, this study is supported *via* funding from Prince Sattam bin Abdulaziz University, project number (PSAU/2025/R/1446).

Funding information: Princess Nourah bint Abdulrahman University Researchers Supporting Project number (PNURSP2025R163), Princess Nourah bint Abdulrahman University, Riyadh, Saudi Arabia. In addition, this study is supported *via* funding from Prince Sattam bin Abdulaziz University, project number (PSAU/2025/R/1446).

Author contributions: A.M.O.: conceptualization, methodology, software, formal analysis, validation, writing – original draft. A.M.G: writing – original draft, data curation, investigation, visualization, validation. U.K: conceptualization, writing – original draft, writing – review and editing, supervision, resources. R.S., S.E: validation, investigation, writing – review and editing, formal analysis; project administration; funding acquisition. All authors have accepted responsibility for the entire content of this manuscript and approved its submission.

Conflict of interest: The authors state no conflict of interest.

Data availability statement: The datasets used and/or analyzed during the current study are available from the corresponding author upon reasonable request.

References

[1] Khan I, Zulkifli R, Chinyoka T, Ling Z, Shah MA. Numerical analysis of radiative MHD gravity-driven thin film third-grade fluid flow with exothermic reaction and modified Darcy's law on an inclined plane. Mech Time-Depend Mater. 2025;29(1):1–18.

[2] Lee TS, Ooi EH, Chang WS, Foo JJ. Augmentation of piezoelectric thin-film flapping velocimetry turbulence strength detection via machine learning. Phys Fluids. 2025;37(1):015117.

[3] Alharbi AF, Usman M, Areshi M, Mahariq I. Nanoconfined multiscale heat transfer analysis of hybrid nanofluid flow with magnetohydrodynamic effect and porous surface interaction. Multiscale and Multidisciplinary Modeling. Exp Des. 2025;8(1):34.

[4] Pal D, Chatterjee D. Impact of Brownian motion and thermophoresis in magnetohydrodynamic dissipative: Radiative flow of chemically reactive nanoliquid thin films on an unsteady expandable sheet in a composite media. Heat Transf. 2025;54(1):941–67.

[5] Obalalu AM, Khan U, Olayemi OA, Zaib A, Ishak A, Sherif ESM. Thermal transport energy performance on tangent hyperbolic hybrid nanofluids and their implementation in concentrated solar aircraft wings. Open Phys. 2024;22(1):20230207.

[6] Khan U, Obalalu AM, Zaib A, Ishak A, Hussain SM, Madhukesh JK, et al. Irreversibility analysis of cross-flow in Eyring–Powell nanofluid over a permeable deformable sheet with Lorentz forces. ZAMM-J Appl Math Mech/Z Angew Math Mech. 2024;e202300835.

[7] Zhang G, Luo J, Sun M, Yu Y, Wang J, Chen B, et al. Effect of soft magnetic particles content on multi-physics field of magnetorheological composite gel clutch with complex flow channel excited by Halbach array arrangement. Compos Part A: Appl Sci Manuf. 2025;188:108576.

[8] Zheng J, Castro J, Liu Y, Oliva A, Pérez-Segarra CD. Study on temperature distribution of vertical liquid falling film heat transfer with Al2O3 nanofluid. Appl Therm Eng. 2024;239:122091.

[9] Jiang M, Tao X, Chen W, Dai Z. An enhanced interface-sharpening algorithm for accurate simulation of underwater explosion in compressible multiphase flow on complex grids. Phys Fluids. 2025;37(1):016112.

[10] Alqurashi MS, Gul H, Ahmad I, Majeed AH, Khalifa HAEW. A study of thermal conductivity enhancement in magnetic blood flow: Applications of medical engineering. Int J Heat Fluid Flow. 2025;112:109719.

[11] Khan MN, Khan AA, Alhowaity A, Masmoudi A, Daradkeh YI, Afikuzzaman M. Computational analysis of magnetized bio-convective partially ionized flow of second-order fluid on a bidirectional porous stretching sheet with Cattaneo–Christov theory. J Comput Des Eng. 2024;11(1):247–60.

[12] Mebarek-Oudina F, Dharmaiah G, Rama Prasad JL, Vaidya H, Kumari MA. Investigation of magnetohydrodynamic Burgers' fluid flow under cylinder stretching: Effects of internal heat generation and absorption. Int J Thermophys. 2025;25:100986. doi: 10.1016/j.ijft.2024.100986.

[13] Nimmy P, Obalalu AM, Nagaraja KV, Madhukesh JK, Khan U, Ishak A, et al. Computational analysis of nanoparticles and waste discharge concentration past a rotating sphere with Lorentz forces. Appl Rheol. 2024;34(1):20240012.

[14] Mebarek-Oudina F, Dharmaiah G, Balamurugan KS, Ismail AI, Saxena H. The role of quadratic-linearly radiating heat source with Carreau nanofluid and exponential space-dependent past a cone and a wedge: a medical engineering application and renewable energy. J Comput Biophys Chem. 2023;22(8):997–1011.

[15] Hussain SM, Khan U, Obalalu AM, Zaib A. Thermal conductivity evaluation of magnetized non-Newtonian nanofluid and dusty particles with thermal radiation. High Temp Mater Process. 2024;43(1):20240063.

[16] Khomenko E, Martínez-Gómez D. MHD waves in the partially ionized plasma: from single to multifluid approach. In Magnetohydrodynamic processes in solar plasmas. Elsevier; 2024. p. 203–71. doi: 10.1016/b978-0-32-395664-2.00011-6.
[17] Gasmi H, Akindele AO, Obalalu AM, Usman AA, Khan U, Yilmaz Y, et al. Electromagnetic control and heat transfer enhancement in exothermic reactions experiencing current density: The study preventing thermal explosions in reactive flow. Appl Rheol. 2024;34(1):20240020.
[18] Dharmaiah G, Mebarek-Oudina F, Prasad JR, Rani CB. Exploration of bio-convection for slippery two-phase Maxwell nanofluid past a vertical induced magnetic stretching regime associated for biotechnology and engineering. J Mol Liq. 2023;391:123408.
[19] Iqbal M, Khan NS, Khan W, Hassine SBH, Alhabeeb SA, Khalifa HAEW. Partially ionized bioconvection Eyring–Powell nanofluid flow with gyrotactic microorganisms in thermal system. Therm Sci Eng Prog. 2024;47:102283.
[20] Jazaa Y, Rehman S, Albouchi F. On the enhancement of heat transport and entropy generation of the thin film flow of partially ionized non-Newtonian hybrid nanofluid. J Taiwan Inst Chem Eng. 2024;157:105412.
[21] Wang Z, Wang S, Wang X, Luo X. Permanent magnet-based superficial flow velometer with ultralow output drift. IEEE Trans Instrum Meas. 2023;72:1–12. doi: 10.1109/TIM.2023.3304692.
[22] Wang G, Sun L, Zhang C. The effect of polyvinylpyrrolidone modified nano-polymers on rheological properties of silicon-based shear thickening fluid. Phys Fluids. 2024;36(7):073108. doi: 10.1063/5.0213620.
[23] Raza J, Mebarek-Oudina F, Ali H, Sarris IE. Slip effects on Casson Nanofluid over a Stretching sheet with activation energy: RSM analysis. Front Heat Mass Transf. 2024;22(4):1017–104.
[24] Ali B, Jubair S, Garayev M, Khalifa HAEW, Kumar A, Shaaban AA. Energy and mass transfer through hybrid nanofluids flow comprised of AA7072-AA7075 nanoparticles subject to magnetic and thermal radiation on stretching surface. J Radiat Res Appl Sci. 2025;18(1):101250.
[25] Fatunmbi EO, Obalalu AM, Khan U, Hussain SM, Muhammad T. Model development and heat transfer characteristics in renewable energy systems conveying hybrid nanofluids subject to nonlinear thermal radiation. Multidiscip Model Mater Struct. 2024;20(6):1328–42.
[26] Shao Y, Pasha AA, Raja MAZ, Arshad Z, Shah Z, Abbasi I, et al. Optimizing the thermo-fluidic properties of ternary hybrid nanofluid for appliance of solar energy through an artificial intelligence integrated numerical solver technique. Chaos, Solitons Fractals. 2025;192:115961.
[27] Mezaache A, Mebarek-Oudina F, Vaidya H, Ramesh K. Impact of nanofluids and porous structures on the thermal efficiency of wavy channel heat exchanger. Int J Therm Sci. 2025;210:109673.
[28] Obalalu AM, Alqarni MM, Odetunde C, Memon MA, Olayemi OA, Shobo AB, et al. Improving agricultural efficiency with solar-powered tractors and magnetohydrodynamic entropy generation in copper–silver nanofluid flow. Case Stud Therm Eng. 2023;51:103603.
[29] Hussein AK, Rashid FL, Rasul MK, Basem A, Younis O, Homod RZ, et al. A review of the application of hybrid nanofluids in solar still energy systems and guidelines for future prospects. Sol Energy. 2024;272:112485.
[30] Al-Turef GA, Obalalu AM, Saleh W, Shah SHAM, Darvesh A, Khan U, et al. Computational study and application of the Hamilton and crosser model for ternary hybrid nanofluid flow past a riga wedge with heterogeneous catalytic reaction. Nano. 2024;20:2450105.
[31] Mishra A, Pathak G. A comparative analysis of MoS_2-SiO_2/H_2O hybrid nanofluid and MoS_2-SiO_2-GO/H_2O ternary hybrid nanofluid over an inclined cylinder with heat generation/absorption. Numer Heat Transfer, Part A: Appl. 2024;85(16):2724–53.
[32] Scott TO, Ewim DRE, Eloka-Eboka AC. Experimental study on the influence of volume concentration on natural convection heat transfer with Al2O3-MWCNT/water hybrid nanofluids. Mater Today: Proc. 2024;105:78–84.
[33] Mebarek-Oudina F, Chabani I, Vaidya H, Ismail AAI. Hybrid-nanofluid magneto-convective flow and porous media contribution to entropy generation. Int J Numer Methods Heat Fluid Flow. 2024;34(2):809–36.
[34] Ali U, Irfan M. Study of gyrotactic motile microorganisms in powell-eyring nanofluid with non-fourier and non-fick's theories. J Therm Anal Calorim. 2024;1–17.
[35] Akram M, Memon AA, Memon MA, Obalalu AM, Khan U. Investigation of a two-dimensional photovoltaic thermal system using hybrid nanofluids and a rotating cylinder. Nanoscale Adv. 2023;5(20):5529–42.
[36] Salawu SO, Yusuf TA, Obalalu AM, Fatunmbi EO. Thermal radiation and propagation of tiny particles in magnetized Eyring–Powell binary reactive fluid with generalized Arrhenius kinetics. Case Stud Therm Eng. 2024;58:104409.
[37] Hashim, Rehman S, Akermi M, Nasr S. Flow and irreversible mechanism of pure and hybridized non-Newtonian nanofluids through elastic surfaces with melting effects. Nonlinear Eng. 2024;13(1):20220361.
[38] Karthik S, Iranian D, Alhazmi H, Khan I, Singh A, Khan MI. Double diffusive on Powell Eyring fluid flow by mixed convection from an exponential stretching surface with variable viscosity/thermal conductivity. Case Stud Therm Eng. 2024;55:104091.
[39] Salawu SO, Yusuf TA, Obalalu AM, Fatunmbi EO, Kareem RA. Internal heating and distribution in electromagnetic powell-Eyring GO − MoS_2/glycerin hybridized nanomaterial with radiation and wall slip conditions. Therm Adv. 2024;1:100006.
[40] Mandal S, Shit GC. Entropy analysis of unsteady magnetohydrodynamic thin liquid film flow of Maxwell nanofluids with variable fluid properties. Mater Chem Phys. 2023;293:126890. doi: 10.1016/j.matchemphys.2022.126890.
[41] Rehman S, Trabelsi Y, Alqahtani S, Alshehery S, Eldin SM. A renovated Jaffrey-Hamel flow problem and new scaling statistics for heat, mass fluxes with Cattaneo–Christov heat flux model. Case Stud Therm Eng. 2023;43:102787.
[42] Wang C. Analytic solutions for a liquid film on an unsteady stretching surface. Heat Mass Transf. 2006;42:759–66.
[43] Abel MS, Mahesha N, Tawade J. Heat transfer in a liquid film over an unsteady stretching surface with viscous dissipation in presence of external magnetic field. Appl Math Model. 2009;33:3430–41.
[44] Afridi MI, Qasim M. Entropy generation and heat transfer in boundary layer flow over a thin needle moving in a parallel stream

in the presence of nonlinear Rosseland radiation. Int J Therm Sci. 2018;123:117–28.

[45] Afridi MI, Qasim M, Khan NA, Makinde OD. Minimization of entropy generation in MHD mixed convection flow with energy dissipation and Joule heating: utilization of Sparrow-Quack-Boerner local non-similarity method. In Defect and diffusion forum. Vol. 387, Switzerland: Trans Tech Publications Ltd; 2018. p. 63–77.

[46] Afridi MI, Qasim M. Comparative study and entropy generation analysis of Cu–H_2O and Ag–H_2O nanofluids flow over a slendering stretching surface. J Nanofluids. 2018;7(4):783–90.

[47] Afridi MI, Dharmaiah G, Prasad JLR, Vedavathi N. Theoretical analysis of MHD Maxwell two phase nano flow subject to viscous dissipation and chemical reaction: A nonsimilar approach. Case Stud Therm Eng. 2025;65:105688.